Optics Letters

Measurement of the topological charge and index of vortex vector optical fields with a space-variant half-wave plate

Gui-Geng Liu,[1] Ke Wang,[1] Yun-Han Lee,[2] Dan Wang,[1] Ping-Ping Li,[1] Fangwang Gou,[2] Yongnan Li,[1] Chenghou Tu,[1,*] Shin-Tson Wu,[2] and Hui-Tian Wang[3,4,5]

[1]*School of Physics and MOE Key Laboratory of Weak Light Nonlinear Photonics, Nankai University, Tianjin 300071, China*
[2]*College of Optics and Photonics, University of Central Florida, Orlando, Florida 32816, USA*
[3]*School of Physics and National Laboratory of Solid State Microstructures, Nanjing University, Nanjing 210093, China*
[4]*Collaborative Innovation Center of Advanced Microstructures, Nanjing University, Nanjing 210093, China*
[5]*e-mail: htwang@nju.edu.cn*
Corresponding author: tuchenghou@nankai.edu.cn

Vortex vector optical fields (VVOFs) refer to a kind of vector optical field with an azimuth-variant polarization and a helical phase, simultaneously. Such a VVOF is defined by the topological index of the polarization singularity and the topological charge of the phase vortex. We present a simple method to measure the topological charge and index of VVOFs by using a space-variant half-wave plate (SV-HWP). The geometric phase grating of the SV-HWP diffracts a VVOF into ±1 orders with orthogonally left- and right-handed circular polarizations. By inserting a polarizer behind the SV-HWP, the two circular polarization states project into the linear polarization and then interfere with each other to form the interference pattern, which enables the direct measurement of the topological charge and index of VVOFs.   © 2018 Optical Society of America

OCIS codes: (050.4865) Optical vortices; (260.5430) Polarization; (230.1950) Diffraction gratings; (260.6042) Singular optics.

https://doi.org/10.1364/OL.43.000823

As an important optical field, optical vortices carrying orbital angular momentum (OAM) have been widely implemented in optical trapping [1], quantum information [2], image processing [3], super-resolution optical microscopy [4], femtosecond micromachining [5], astronomical detection [6,7], and so on. The phase front of a scalar vortex field (SVF) is expressed as $\exp(il\phi)$, where l is the topological charge (TC) of the phase vortex and ϕ is the azimuthal angle. For an optical vortex, each photon carries an OAM of $l\hbar$ so that l needs to be an integer [8]. However, the TC of an optical vortex or the average OAM per photon can also be fractional [9–11]. The measurement of the TC has been conventionally done by the interference with its mirror image [12] or a reference optical field [13,14]. These measurements often require a complex and precise optical

setup. To facilitate the characterization, various kinds of optical elements have been proposed for measuring the TC or the OAM, such as a single or a double slit [15,16], a triangular aperture [17], a sectorial screen [18], an annular aperture [19], a tilted convex lens [20], a wedged optical flat [21], a cylindrical lens [22,23], and an angular double slit [24]. Those optical elements are able to measure both the integral [15–22] and fractional [23,24] TCs, but they were limited to explore SVFs.

Vector optical fields (VOFs) with an azimuth-variant polarization and a helical phase front, known as vortex vector optical fields (VVOFs), are also of great interest for applications, especially in optical communications [25,26]. The polarization singularity of the VVOFs has been characterized by the topological index (TI) [27]. To the best of our knowledge, the measurement of both the TCs and TIs for VVOFs is seldom involved, and the feasibility to measure them by using the above-mentioned optical elements has not been investigated.

In this Letter, we propose a new and simple method to measure the TCs and TIs of VVOFs by using a space-variant half-wave plate (SV-HWP). Both the integral and fractional TCs can be measured directly and quantitatively. The TIs of VVOFs can also be characterized simultaneously. Indeed, SVFs and VOFs can be considered as two special cases of VVOFs, so that our method is also able to determine their TCs and TIs.

The experimental setup is shown in Fig. 1. The input optical field, which will be characterized, can be a SVF, a VOF, or a VVOF. The input optical field propagating along the z-axis is normally incident onto a SV-HWP placed in the $z = 0$ plane. The SV-HWP used here is a liquid-crystal-based SV-HWP [28,29], and has been used in virtual and augmented realities [30,31]. The input optical field can be expressed by the Jones matrix, as a combination of the left- and right-handed circularly polarized (LCP and RCP) components:

$$E_{\text{in}}|_{z=0} = E_l[1, +i]^T + E_r[1, -i]^T, \tag{1}$$
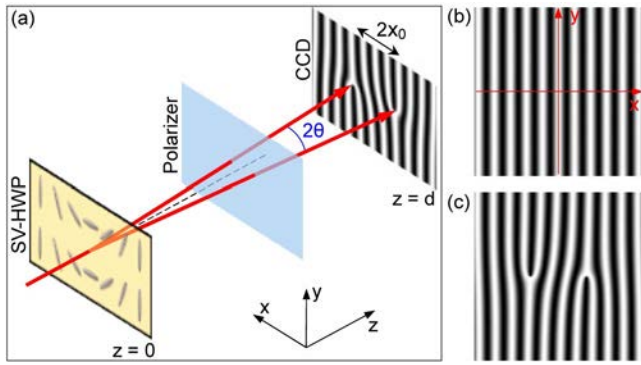
Fig. 1. (a) Optical setup to measure the TC of an input optical field. (b) Detected interference pattern under the incidence of a linearly polarized PW. (c) Detected interference pattern under the incidence of a SVF with $l = 1$.

where E_l and E_r denote the complex amplitudes of the LCP and RCP components, respectively. When the input optical field expressed in Eq. (1) passes through a *space-invariant* half-wave plate at an azimuthal angle ϕ (which is an angle between the fast axis and the x-axis), the output can be written as

$$\tilde{E}_{\text{out}}|_{z=0} = E_l[1, -i]^T e^{+i2\phi} + E_r[1, +i]^T e^{-i2\phi}. \quad (2)$$

Clearly, the handedness of polarization is flipped and any output circularly polarized optical field accumulates simultaneously a geometric phase of $\exp(+i2\phi)$ or $\exp(-i2\phi)$. For the SV-HWP we used, ϕ is set to be space-variant and has a form of $\phi = 2\pi f x$, where f is the spatial frequency and set to be 1.4 mm^{-1} in our experiments. The space-variant optic axis of the liquid crystal can be easily realized through the photo-alignment technique [32]. The refractive index and cell thickness of the liquid-crystal-based SV-HWP are carefully tuned to make the SV-HWP act as a half-wave plate at a wavelength of $\lambda = 633$ nm. Under the incidence of optical field in Eq. (1), the optical field output just from the SV-HWP can be expressed as

$$E_{\text{out}}|_{z=0} = E_l[1, -i]^T e^{+i4\pi f x} + E_r[1, +i]^T e^{-i4\pi f x}. \quad (3)$$

We can easily see from Eq. (3) that the LCP and RCP components of the output optical field are flipped (with respect to the input field) in handedness, and accumulate synchronously the linear-variant geometric phases of $\exp(\pm i4\pi f x)$, respectively. In fact, the two components of the output optical field are the ± 1 orders diffracted by the linear-variant geometric phase grating of the SV-HWP, respectively. The diffraction angle can be expressed as $\theta = 2f\lambda$, which is approximately 0.1° in our case. After the SV-HWP, the ± 1 orders will interfere with each other, and consequently a particular interference field will be generated. The interference pattern depends on the amplitude, phase, and polarization distributions of the input field. In particular, the polarization complicates not only the interference pattern itself but also its analysis. To resolve the polarization structure of the interference field, we insert a linear polarizer behind the SV-HWP, the LCP and RCP components diffracted from the SV-HWP are projected into the linear polarization along the x-axis, and then interference with each other in the plane of a CCD camera placed with a distance of d away from the SV-HWP. The interference field detected by the CCD should be written as

$$E_{\text{CCD}} = J_p E_{\text{out}}|_{z=d}$$
$$= E_l(x - x_0, y)e^{+i4\pi f x} + E_r(x + x_0, y)e^{-i4\pi f x}, \quad (4)$$

where $x_0 = d \tan \theta$ is the displacement of the ± 1 orders in the x-axis and J_p is the Jones matrix of a polarizer oriented along the x-axis.

When the input optical field in Eq. (1) is the x-polarized plane wave (PW) with an uniform amplitude of E_0, E_r and E_l in Eqs. (1) or (4) should have $E_r = E_l = \frac{1}{2}E_0$. Based on Eq. (4), the interference field detected by the CCD is expressed as

$$E_{\text{CCD}}^{\text{PW}} = \frac{1}{2}E_0(e^{+i4\pi f x} + e^{-i4\pi f x}), \quad (5)$$

which exhibits a parallel interference fringe shown in Fig. 1(b).

When the input optical field is a x-polarized SVF with an amplitude of E_0 and a helical phase of $\exp(il\phi)$, thus E_r and E_l in Eqs. (1) or (4) should have $E_l = E_r = \frac{1}{2}E_0 \exp(il\phi) = \frac{1}{2}E_0 \exp[il \arctan(y/x)]$, where l is the TC of the phase vortex and $\phi = \arctan(y/x)$. So, under the incidence of a SVF, the interference field detected by the CCD has the following form:

$$E_{\text{CCD}}^{\text{SVF}} = \frac{1}{2}E_0 e^{i[l \arctan\frac{y}{x-x_0} + 4\pi f x]} + \frac{1}{2}E_0 e^{i[l \arctan\frac{y}{x+x_0} - 4\pi f x]}. \quad (6)$$

For instance, as shown in Fig. 1(c), when the input SVF has a TC of $l = 1$, the two forks contained in the interference pattern, i.e., a downward fork with its center located at $(x_0, 0)$ and a upward fork with its center located at $(-x_0, 0)$, respectively, are centrosymmetric, which means to be symmetric with respect to the origin of the xy plane [the center of the image in Fig. 1(c)]. From Fig. 1(c) and Eq. (6), the downward fork centered at $(x_0, 0)$ can be considered as the interference between a PW and a SVF with the TC of $|l'| = l = 1$, which is expressed by the first term of Eq. (6); while the upward fork centered at $(-x_0, 0)$ is from the interference between a PW and a SVF with its TC of $|l''| = l = 1$, as expressed by the second term of Eq. (6). We define that when the fork pattern in the region of $x > 0(x < 0)$ is downward (upward), the sign of $l'(l'')$ is positive (positive), and vice versa. Based on the above definition, we have $l' = l = 1$ and $l'' = l = 1$ in Fig. 1(c).

Figures 2 and 3 show the interference patterns under the incidence of SVFs with positive TCs ($l = +1, +2, +3, +6$) and negative TCs ($l = -1, -2, -3, -6$), respectively. Clearly, the experimental results are in good agreement with the theoretical ones for not only the positive (Fig. 2) but also the negative TCs (Fig. 3). Any interference pattern under the incidence of SVF exhibits a dual-fork and centrosymmetric structure. For $l = \pm 1, \pm 2, \pm 3$, the distance d between the SV-HWP and
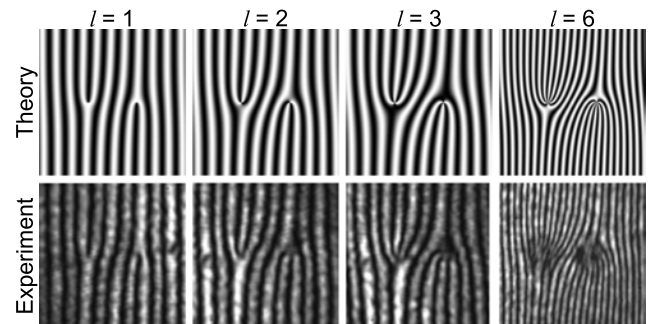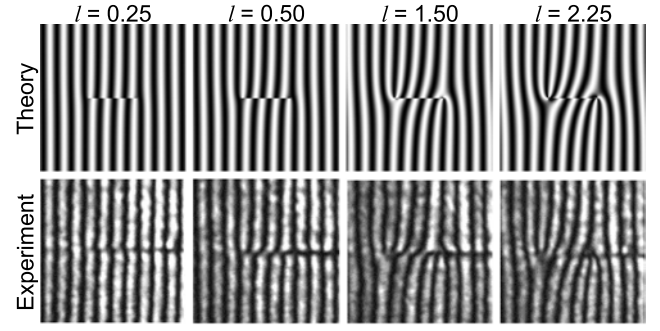

Fig. 2. Detected interference patterns under the incidence of SVFs with integral TCs ($l = +1, +2, +3, +6$, respectively).

Fig. 3. Detected interference patterns under the incidence of SVFs with integral TCs ($l = -1, -2, -3, -6$, respectively).
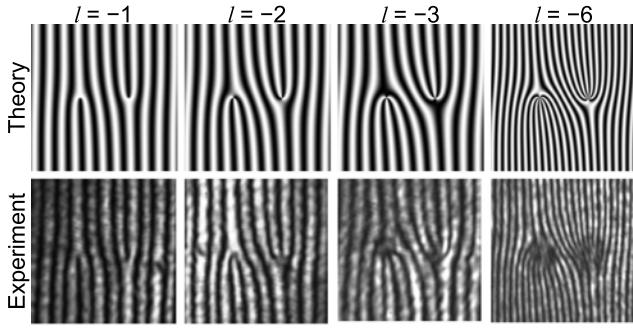
Fig. 4. Detected interference patterns under the incidence of SVFs with fractional TCs ($l = 0.25, 0.50, 1.50, 2.25$, respectively).

the CCD is set to be 150 mm. For $l = \pm 6$, d is set to be 300 mm. As d increases, the displacement of x_0 will increase accordingly, so that there will be more fringes between ± 1 orders along the x-axis. In our case, the number of fringes between ± 1 orders is doubled so that the increased bright fringes can be counted more clearly. For the positive or negative l, the two forks in any interference pattern have the same number of bifurcations, which increase along with $|l|$. For the positive l (shown in Fig. 2), the interference patterns for the downward fork [with its center located at $(x_0, 0)$] and the upward fork [with its center located at $(-x_0, 0)$] indicate $l' = +1, +2, +3, +6$ and $l'' = +1, +2, +3, +6$, respectively. While for the negative l (shown in Fig. 3), the upward fork [with its center located at $(x_0, 0)$] and the downward fork [with its center located at $(-x_0, 0)$] show $l' = -1, -2, -3, -6$ and $l'' = -1, -2, -3, -6$, respectively. Based on the above definition, therefore, we can assert that the TCs of the input SVFs in Fig. 2 (Fig. 3) are equal to $l = l' = l'' = +1, +2, +3, +6$ ($l = l' = l' = -1, -2, -3, -6$), respectively.

In the above, only the integral TCs have been involved, and its magnitude and sign can be determined through the number and orientation of the fork fringes. For the OAM-carrying SVF, the TC can also be fractional, which can be presented by the superposition of a series of integral OAM-carrying SVFs. In our experiment, the feasibility of measuring the fractional TC has also been proved. Figure 4 shows the theoretical and experimental results under the incidence of SVFs with the fractional TCs of $l = 0.25, 0.50, 1.50, 2.25$, respectively. For the fractional OAM carried by the SVF, the phase step in the $+x$ direction is discontinuous, which refers to a theoretical singular line in the input field. As propagating in the air, the singular line of the input SVF will evolve into an obvious dark line [9], which can be explained by evanescent waves at phase discontinuity [10]. In the detected interference pattern, there also appears a dark strip starting from the left singularity. As shown in Fig. 4, when l is changed from $l = 0$ into $l = 0.25$, the fringes between two singularities are disconnected at $y = 0$, and the fringes in the upper part with $y > 0$ shift a quarter of the fringe period toward the $+x$ direction with respect to the fringes in the lower part with $y < 0$. When $l = 0.50$, the fringes will shift a half of the fringe period. For $l = 1.50$ ($l = 2.25$), the fringes increase one (two) fringe(s) at the singularities and have a half (a quarter) of the fringe period. Therefore, we can determine from Fig. 4 that $|l'| = 0.25, 0.50, 1.50, 2.25$ in the fork located at $(x_0, 0)$ and $|l''| = 0.25, 0.50, 1.50, 2.25$ in the fork at $(-x_0, 0)$, respectively. In addition, we can conclude from the

orientations of forks that the signs of TCs of phase vortices located at $(x_0, 0)$ and $(-x_0, 0)$ are all positive, based on the above definition. Therefore, the measured TCs of the input SVFs are in complete agreement with the default values, i.e., $l = l' = l'$. By this way, the fractional TC can be obtained quantitatively through measuring the displacement of fringes. The resolution of the measured TC, which is about 0.1 in our experiment, is determined and limited by the quality of the experimental patterns.

For an azimuth-variant VOF, its polarization distribution should be characterized by the TI of polarization singularity [27,33]. The VVOFs are a kind of VOFs with an azimuth-variant polarization and a helical phase, simultaneously. Thus, a VVOF should be characterized by the TI (m) and the TC (l). We now explore the measurement of TI (m) and TC (l) of the VVOF. To the best of our knowledge, the measurement of the OAM limits only to SVFs in previous publications. Here the feasibility to measure the TC of the SVF, the TI of the VOF, and the TI and TC of the VVOF is proved by our method. Under the incidence of VVOF (with $E_{\text{VVOF}} = E_0 \exp(il\phi)[\cos(m\phi), \sin(m\phi)]^T$), the complex amplitudes, E_l and E_r, in Eqs. (1) or (4) should be expressed as $E_l = \frac{1}{2} E_0 \exp[i(l-m)\phi]$ and $E_r = \frac{1}{2} E_0 \exp[i(l+m)\phi]$, respectively. With Eq. (4), the interference field detected by the CCD is expressed as

$$E_{\text{CCD}}^{\text{VVOF}} = \frac{1}{2} E_0 e^{i[(l-m)\arctan\frac{y}{x-x_0}+4\pi f x]}$$
$$+ \frac{1}{2} E_0 e^{i[(l+m)\arctan\frac{y}{x+x_0}-4\pi f x]}. \quad (7)$$

In fact, the first [second] term indicates the fork pattern caused by the interference between a PW and a SVF with its center located at $(x_0, 0)$ [$(-x_0, 0)$] and a TC of $l' = l - m$ [$l'' = l + m$]. Figure 5 (Fig. 6) shows the theoretical and experimental results under the incidence of VVOFs with $m = 1$ ($m = 2$) for four TCs, i.e., $l = 0, -0.5, -1, -2$, respectively. In the case of $l = 0$, the input VVOF degenerates into a traditional VOF without a phase vortex. As a result, the detected dual-fork interference pattern is symmetric about the y-axis, where one fringe bifurcates into two (three) at the two singularities, as shown in the first column of Fig. 5 (Fig. 6). In particular, the two forks in the first columns of Figs. 5 and 6 are upward under the incidence of a traditional VOF, which is completely different from the interference patterns under the incidence of SVFs, as shown in Figs. 2–4. Based on the above definition, in the first column of Fig. 5 (Fig. 6), we have $l' = -1$ ($l' = -2$)
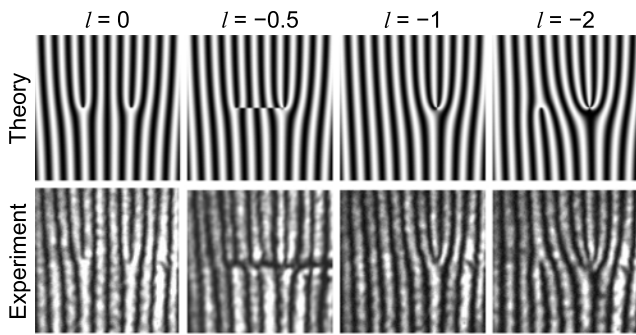
Fig. 5. Detected interference patterns under the incidence of VVOFs for $l = 0, -0.5, -1, -2$ when $m = 1$.
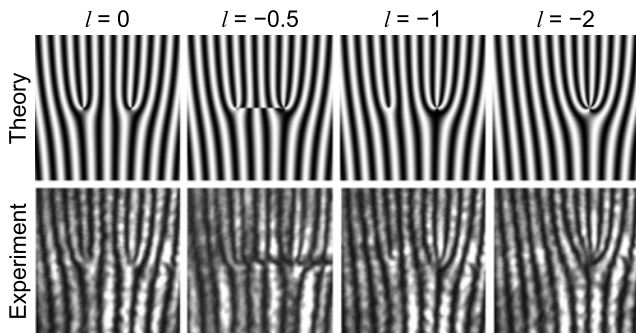
Fig. 6. Detected interference patterns under the incidence of VVOFs for $l = 0, -0.5, -1, -2$ when $m = 2$.

and $l'' = 1$ ($l'' = 2$). For the cases of $l \neq 0$ and $m \neq 0$ in the other three columns of Fig. 5 (Fig. 6), i.e., under the incidence of VVOFs, the fork structures at the two singularities have different bifurcation numbers. Based on the bifurcation numbers at the singularities, we can determine the TCs and TIs of VVOFs. As is well known, the increased fringes at each singularity are exactly equal to the corresponding TC. Therefore, the fork structures located at the region of $x > 0$ in the second, third, and fourth columns of Fig. 5 (Fig. 6) correspond to $l' = -1.5, -2, -3$ ($l' = -2.5, -3, -4$), respectively. The fork structures located at the region of $x < 0$ in the second, third, and fourth columns of Fig. 5 (Fig. 6) correspond to $l'' = 0.5, 0$ and -1 ($l'' = 1.5, 1,$ and 0), respectively.

With $l' = l - m$ and $l'' = l + m$, we have $l = (l' + l'')/2$ and $m = (l'' - l')/2$. Thus we can deduce that $(l, m) = (0, 1)$, $(l, m) = (-0.5, 1)$, $(l, m) = (-1, 1)$, and $(l, m) = (-2, 1)$, from the first, second, third, and fourth columns of Fig. 5, respectively. Similarly, we also have $(l, m) = (0, 2)$, $(l, m) = (-0.5, 2)$, $(l, m) = (-1, 2)$, and $(l, m) = (-2, 2)$, from the first, second, third, and fourth columns of Fig. 6, respectively. Clearly, the TC (l) and the TI (m), deduced from the experimentally measured interference patterns, are the default values of the input optical fields.

In summary, we presented and validated a method to measure the TCs and TIs based on the geometric phase grating of a space-variant half-wave plate. This method is applicable to the scalar vortex fields, vector optical fields, and vortex vector optical fields. This method allows us to characterize both the magnitudes and signs of TCs and TIs, quantitatively and directly, no matter

whether the TCs are integral or fractional. Compared with other methods, this method is very simple, effective, and has great potential in scientific and practical applications. In particular, the space-variant half-wave plate can be used to control the polarization of light and to generate the vector optical fields.

REFERENCES

1. M. Padgett and R. Bowman, Nat. Photonics **5**, 343 (2011).
2. A. Nicolas, L. Veissier, L. Giner, E. Giacobino, D. Maxein, and J. Laurat, Nat. Photonics **8**, 234 (2014).
3. G. Situ, G. Pedrini, and W. Osten, J. Opt. Soc. Am. A **26**, 1788 (2009).
4. S. W. Hell and J. Wichmann, Opt. Lett. **19**, 780 (1994).
5. K. Ladavac and D. G. Grier, Opt. Express **12**, 1144 (2004).
6. G. A. Swartzlander, Opt. Lett. **26**, 497 (2001).
7. G. Foo, D. M. Palacios, and G. A. Swartzlander, Opt. Lett. **30**, 3308 (2005).
8. L. Allen, M. W. Beijersbergen, R. J. C. Spreeuw, and J. P. Woerdman, Phys. Rev. A **45**, 8185 (1992).
9. M. V. Berry, J. Opt. A **6**, 259 (2004).
10. S. N. Alperin and M. E. Siemens, Phys. Rev. Lett. **119**, 203902 (2017).
11. G. Gbur, Optica **3**, 222 (2016).
12. M. Harris, C. A. Hill, P. R. Tapster, and J. M. Vaughan, Phys. Rev. A **49**, 3119 (1994).
13. V. Y. Bazhenov, M. V. Vasnetsov, and M. S. Soskin, JETP Lett. **52**, 429 (1990).
14. I. V. Basistiy, M. S. Soskin, and M. V. Vasnetsov, Opt. Commun. **119**, 604 (1995).
15. Q. S. Ferreira, A. J. Jesus-Silva, E. J. Fonseca, and J. M. Hickmann, Opt. Lett. **36**, 3106 (2011).
16. H. I. Sztul and R. R. Alfano, Opt. Lett. **31**, 999 (2006).
17. J. M. Hickmann, E. J. S. Fonseca, W. C. Soares, and S. Chávez-Cerda, Phys. Rev. Lett. **105**, 053904 (2010).
18. R. Chen, X. Zhang, Y. Zhou, H. Ming, A. Wang, and Q. Zhan, Appl. Opt. **56**, 4868 (2017).
19. C. S. Guo, L. L. Lu, and H. T. Wang, Opt. Lett. **34**, 3686 (2009).
20. P. Vaity, J. Banerji, and R. P. Singh, Phys. Lett. A **377**, 1154 (2013).
21. B. Khajavi and E. J. Galvez, Opt. Lett. **42**, 1516 (2017).
22. E. Abramochkin and V. Volostnikov, Opt. Commun. **83**, 123 (1991).
23. S. N. Alperin, R. D. Niederriter, J. T. Gopinath, and M. E. Siemens, Opt. Lett. **41**, 5019 (2016).
24. J. Zhu, P. Zhang, D. Fu, D. Chen, R. Liu, Y. Zhou, G. Hong, and F. Li, Photon. Res. **4**, 187 (2016).
25. G. Milione, M. P. Lavery, H. Huang, Y. Ren, G. Xie, T. A. Nguyen, E. Karimi, L. Marrucci, D. A. Nolan, R. R. Alfano, and A. E. Willner, Opt. Lett. **40**, 1980 (2015).
26. G. Milione, T. A. Nguyen, J. Leach, D. A. Nolan, and R. R. Alfano, Opt. Lett. **40**, 4887 (2015).
27. J. G. Gregory, in *Singular Optics* (CRC Press, 2017), pp. 185–258.
28. S. R. Nersisyan, N. V. Tabiryan, D. M. Steeves, and B. R. Kimball, Opt. Photon. News **21**(3), 40 (2010).
29. C. Provenzano, P. Pagliusi, and G. Cipparrone, Appl. Phys. Lett. **89**, 121105 (2006).
30. Y. H. Lee, G. Tan, T. Zhan, Y. Weng, G. Liu, F. Gou, F. Peng, N. V. Tabiryan, S. Gauza, and S. T. Wu, Opt. Data Process. Storage **3**, 79 (2017).
31. H. Chen, Y. Weng, D. Xu, N. V. Tabiryan, and S. T. Wu, Opt. Express **24**, 7287 (2016).
32. M. Schadt, H. Seiberle, and A. Schuster, Nature **381**, 212 (1996).
33. X. L. Wang, J. P. Ding, W. J. Ni, C. S. Guo, and H. T. Wang, Opt. Lett. **32**, 3549 (2007).